A γ-Ray Detector Based on a 3" LaBr$_3$:Ce:Sr Crystal With SiPM Readout for 80 keV–16 MeV Energy Range With Position Sensitivity for Doppler Correction

Marco Agnolin, Davide Di Vita, *Member, IEEE*, Giacomo Borghi, *Member, IEEE*,
Marco Carminati, *Senior Member, IEEE*, Franco Camera, Oliver Wieland, Bénédicte Million,
Agnese Giaz, Constantin Mihai, Andrei Turturica, Cristian Costache, Ruxandra Borcea,
Pär-Anders Söderström, Rebeca Sara Ban, and Carlo Fiorini, *Senior Member, IEEE*

Abstract—We report the validation in an extended energy range (80 keV – $\simeq$16 MeV) of the GAMMA detector, a high-dynamic range, high-resolution, gamma-ray spectrometer for nuclear physics applications based on a 3" co-doped lanthanum bromide (LaBr$_3$:Ce:Sr) crystal (73 ph/keV conversion efficiency, 25 ns decay time) coupled to 144 NUV-HD silicon photomultipliers (SiPMs). The detector shows state-of-the-art energy resolution along the entire range thanks to the automatic gain switching feature [adaptive gain control (AGC)] of the custom application-specific integrated circuits (ASICs) employed in the system. To the best of our knowledge, this is the first time that SiPMs have been used to measure such high energy together with a wide dynamic range and excellent energy resolution (2.7% at 662 keV). In addition, the pixelated nature of the SiPMs detectors, combined with machine learning (ML) algorithms, can be exploited to reconstruct the position of the first interaction of the gamma rays inside the scintillation crystal. Previous measurements with a ^{137}Cs collimated source have achieved a spatial resolution better than 2 cm. This performance in position sensitivity has been used to compensate for the relativistic Doppler broadening effects of gamma rays at 15.110(3) MeV emitted by a carbon nucleus moving at relativistic speed (v/c $\simeq$ 0.05) resulting from a boron-on-deuterium reaction, improving the FWHM resolution of the peak by 15%, which is in agreement with the theoretical expectation.

Index Terms—Doppler correction, lanthanum bromide, relativistic Doppler broadening, scintillators, silicon photomultipliers (SiPMs).

I. INTRODUCTION

IN SEVERAL areas of physics such as gamma spectroscopy with state-of-the-art scintillators [1], [2], [3], [4], [5], SiPMs are substituting traditional photomultiplier tubes (PMTs) as photodetectors. This is a result of their compactness, low voltage requirement [6], excellent energy resolution capabilities, and insensitivity to magnetic fields [7], as well as the potential for achieving some position sensitivity (Section IV-D and [8], [9]). In addition, as the SiPMs could be assembled in tiles, they can cover large surfaces (namely several cm^2 or even m^2 [10], [11]). They can, therefore, be coupled to large scintillators for the detection of medium- or high-energy gamma-rays and are particularly suited for applications where position sensitivity is needed.

In this article, we present and discuss the energy spectrum of monochromatic 15.110(3) MeV γ-radiation, together with several other γ-lines in an extended energy range, measured using a large volume 3" $\times$ 3" co-doped LaBr$_3$:Ce:Sr crystal coupled to an array of 144 SiPMs arranged in a 12 $\times$ 12 matrix by means of silicone optical grease (Saint Gobain BC 630). The 15.11 MeV γ rays were produced using the fusion reaction ^{11}B + D performed at the 9 MV Tandem Accelerator laboratory of IFIN-HH at Măgurele (Bucharest) in Romania. The detector was first calibrated using standard low-energy calibration sources and a PuBeNi composite source [12], [13]. The 15.11 MeV γ rays were measured with and without a lead vertical collimator 1–2 cm large and 10 cm thick. We also present: 1) a comparison between a gamma-ray
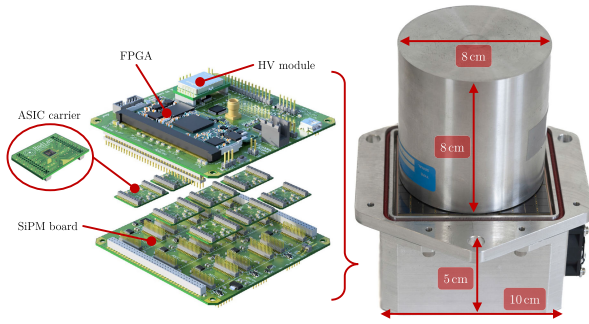
Fig. 1. Pictures of the GAMMA detector. The 8×8 cm cylinder is the LaBr$_3$:Ce:Sr crystal and constitutes the largest part of the instrument. The $5 \times 10 \times 10$ cm part contains the SiPM array and all the electronics.

spectrum in the energy range from 80 keV to $\simeq$16 MeV measured using a fixed gain with that measured using an event-by-event variable gain (the automatic gain switching system called adaptive gain control (AGC) detailed in [2] and [14]) and 2) the measurement of the non-linearity of the SiPMs system in the energy range 0.08–$\simeq$16 MeV and a technique to correct it. This work can be considered as the continuation of the activity reported in [2] as the system we have used is the same 144-SiPMs 3" readout module (from now identified as the GAMMA detector), which was therein described. It is important to stress the point that, with the name GAMMA, we refer to the ensemble of the LaBr$_3$:Ce:Sr crystal, the matrix of SiPMs, and the associated custom application-specific integrated circuits (ASICs) and electronics.

In Section II, we discuss the GAMMA detector, while in Section III, we discuss the experimental procedure used. In Section IV-A, we present the energy performance of the detector and AGC system; in this section, we will also show the energy spectrum and the performance using a fixed gain compared to the one using the AGC. In Sections IV-B and IV-C, we discuss the measured non-linearity of the SiPMs, and some analyses made possible by the 144 independent SiPM channels of the detector. In Section IV-D, we show the results of a very simple position-sensitive algorithm (based on a machine learning (ML) approach) for the reduction of the relativistic Doppler broadening [15], [16].

II. GAMMA DETECTOR

The GAMMA detector (Fig. 1) [2] is a high-resolution, high-dynamic range, SiPM-based system for indirect conversion gamma spectroscopy and imaging. It is based on a 3" $\times$ 3" cylindrical co-doped lanthanum bromide crystal (LaBr$_3$:Ce:Sr) readout by 144 NUV-HD silicon photomultipliers (SiPMs) from FBK [6] with 30 μm cell size. Nine custom 16-channel ASICs [14] provide 144 readout channels for SiPMs' current signal integration; the output voltages of the ASICs are then digitized by external ADCs, and the values are collected by the FPGA-based DAQ for further processing and transfer to the host PC.

The 3" $\times$ 3" LaBr$_3$:Ce:Sr crystal was bought from Saint Gobain for which the company declared an energy resolution (measured using a PMT) of 2.8% at 662 keV and 2% at 1332 keV.

A custom bias voltage module allows the correct operation of SiPMs at any temperature, effectively compensating for

gain drifts due to temperature variations with a sensibility of 0.02 °C (the "Auto HV" feature). The temperature compensating system is active up to several °C of variation. Since the temperature is uniform across the entire matrix, there is no need to compensate each SiPM gain independently; thus, a common bias is used.

The system is able to reach state-of-the-art energy resolution [2], [5] with an energy dynamic range that starts from a few tens of keV up to 30 MeV in a single measurement without saturation. Interaction point position reconstruction has also been demonstrated with a spatial resolution better than 2 cm [8]. This spatial resolution could be enough for relativistic Doppler effect correction [16].

III. EXPERIMENTAL SETUP

The measurement was performed in the 9 MV FN Pelletron Tandem Accelerator laboratory at the IFIN-HH Institute for R&D in Physics and Nuclear Engineering in Măgurele (Bucharest, Romania) [17], [18], [19]. The 15.110(3) MeV γ rays were produced in the ground state decay of a 1^+ nuclear level of ^{12}C. This level in ^{12}C is below the neutron and the proton separation energy ($S_n = 18.7$, $S_p = 15.9$ MeV) and, once populated, it decays directly to the ground state with a probability of the order of $\simeq$90% (there is also an α decay branch but it is very small) [20], [21], [22]. The excited nucleus of ^{12}C was created from the one-neutron evaporation channel of excited ^{13}C, which was in turn populated in the fusion-evaporation reaction between a beam of ^{11}B at 19 MeV of energy and D. The fusion cross section of the reaction is approximately 900 mb [23], [24]. Because of the inverse kinematic of the used reaction, the residues are expected to move with a v/c of the order of 5%. Therefore, in the uncollimated spectra, a small but not negligible Doppler broadening effect should be present (Section IV-D).

In this measurement, a beam of ^{11}B was used with an intensity of approximately 7 enA (electrical nanoampere). As the ^{11}B beam was in a 4+ charge state, the intensity of the beam was 1.75 particle nanoampere (pnA). A gold absorber with a thickness of 5.3 mg/cm^2 was placed in front of the target to degrade the beam from 25 MeV down to 19 MeV. The target consisted of 700 μg/cm^2 of CD$_2$ on a tantalum backing. The tantalum backing completely stops the ^{11}B beam. The target holder was made of thick (1 mm) copper to avoid overheating of the target due to the incident beam.

A vertical lead collimator composed of 10-cm long lead bricks was also used during the measurement and placed in front of the GAMMA detector (Fig. 2). The detector could slide with a step motor orthogonally to the direction of the incident 15.11 MeV γ radiation. The slide movement made it possible to illuminate different parts of the detector while keeping the collimator fixed. A total of nine different runs were performed, each several hours long. One run was performed without the lead collimator, five runs used a collimation width of 1 cm [Fig. 3(a)], and three runs used a collimation width of 2 cm [Fig. 3(b)]. In the runs with 1 cm collimation width, the central part, the right, and left part, and the extreme right and extreme left part were illuminated (Section IV-D); as visible in the figure, due to an initial positioning offset, the five slices are not perfectly equally spaced. In the runs with 2 cm collimation
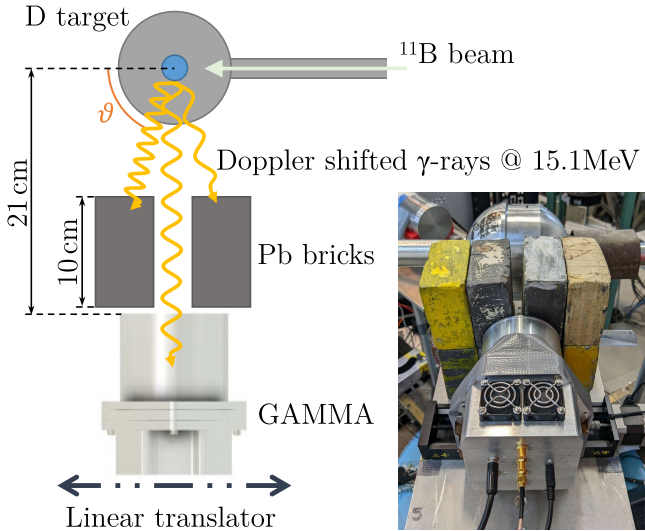
Fig. 2. Schematic top view of the measurement setup. The detector is mounted on a linear translator stage to allow movement behind the lead collimator in order to illuminate different portions of the crystal at a time. For the uncollimated measurement, the lead bricks have been removed. The crystal surface is placed about 21 cm away from the target at 90° angle to maximize the Doppler effect. On the right, a photo of the detector setup is shown.

width, only the central, the right, and the left parts of the crystal were illuminated.

The front face of the GAMMA detector, namely the crystal surface opposite to the SiPM matrix, was placed at approximately 21 cm from the target at 90° relative to the beam direction to maximize the Doppler broadening (Fig. 2).

IV. EXPERIMENTAL RESULTS

A. Adaptive Gain Control

A 30-min acquisition simultaneously using uncollimated ^{133}Ba, ^{137}Cs, ^{60}Co, and PuBeNi radioactive sources and ^{11}B + D reaction has been performed to test the spectroscopy performance of the system. The obtained spectrum spans from the 81 keV γ-ray resulting from ^{133}Ba decay up to the 15.11 MeV γ-ray produced in the boron on deuterium reaction; the endpoint of the energy spectrum is around 30 MeV and at energies higher than 15 MeV, events induced by cosmic rays are visible. To validate the ability of the system to achieve a very large dynamic range, maintaining a resolution of 2.7% at the 662 keV peak of ^{137}Cs, the automatic-gain-switching feature (AGC [14]) of the custom ASICs has been enabled. This feature automatically selects the most appropriate gain [i.e., connecting different integration capacitances for a total value of 1 pF (G1), 5 pF (G2), or 12 pF (G3)] individually for each SiPM channel. For example, if a scintillation event occurs very close to the SiPM matrix, the SiPMs directly below the event will use a low gain to avoid saturation due to a large number of photons, while the further away SiPMs that receive less light will use higher gain. A direct comparison between the AGC spectrum and the one obtained with the lowest fixed gain is visible in Fig. 4(a), as well as the corresponding energy resolutions for the low-energy part in the inset. From Table I, it is clear that the AGC feature ensures a better resolution.
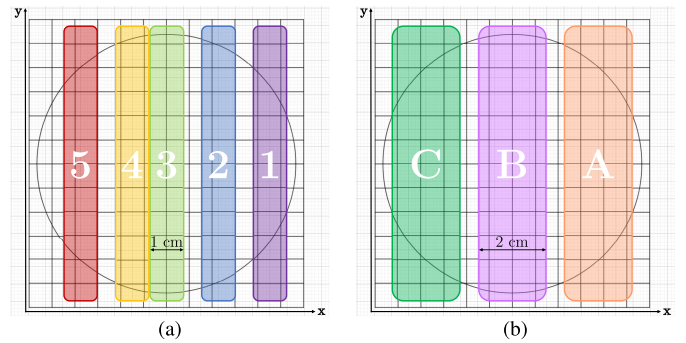

Fig. 3. Eight vertical labeled slices represent the illuminated regions of the crystal (represented by the black circumference over the SiPMs grid). (a) Five slices of 1 cm width are not equally distributed due to a problem in the positioning of the detector. (b) Three slices of 2 cm width.

TABLE I
SUMMARY OF THE LOW-ENERGY RESOLUTIONS
OF AGC AND G3 (LOWEST FIXED GAIN) SPECTRA

| Energy [keV]	Adaptive gain (AGC)	Lowest fixed gain (G3)
276	5.4%	7.2%
303	4.5%	6.2%
356	3.9%	5.1%
384	3.6%	n/a
511	3.1%	3.8%
662	2.7%	3.3%
1173	2.0%	2.2%
1332	1.8%	2.0%
2223	1.7%	1.9%

In Fig. 4(b), the magnification of the low energy portion of the spectrum shown in Fig. 4(a) highlights the differences between the two gain modalities. In particular, it can be seen how the peak at 384 keV of barium is almost invisible in the fixed gain one. To our knowledge, these are the first measurements with a device based on SiPMs that include such a large energy range with state-of-the-art resolution in a single spectrum. A precise calibration procedure is needed to reconstruct the spectrum from the raw data when AGC mode is employed. In particular, the mismatch between the ideal value and the real one in the capacitances of the gated integrator (GI) filter constituting the three different gains needs to be calculated. Moreover, also the voltage reference V_{BL} of the GI, which constitutes the baseline value read by the ADC in the absence of scintillation events, needs to be measured and correctly subtracted before merging the data of different gains. The capacitance ratios have been assessed through a custom current pulser that mimics the current from the SiPMs. Thanks to a one-time fine-tuning of all these parameters, it has been possible to obtain a spectrum matching the one of a fixed gain acquisition.

An analysis of the events captured at four different energies with AGC enabled has been performed. The result is shown in Fig. 5 and highlights the gains utilization percentage for the selected peaks. At low energies, the highest gain G1 is generally used. Instead, when the energy rises, the intermediate gain G2 and the lowest gain G3 kick in. This proves the ability of the system to select event-by-event and SiPM-by-SiPM the correct gain according to the number of incident photons. The adoption of the AGC technique allows to achieve the best
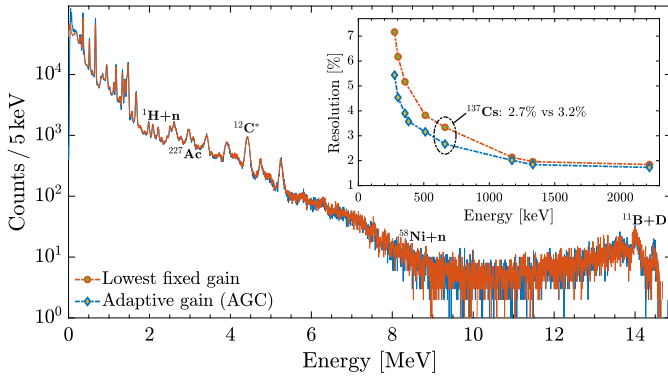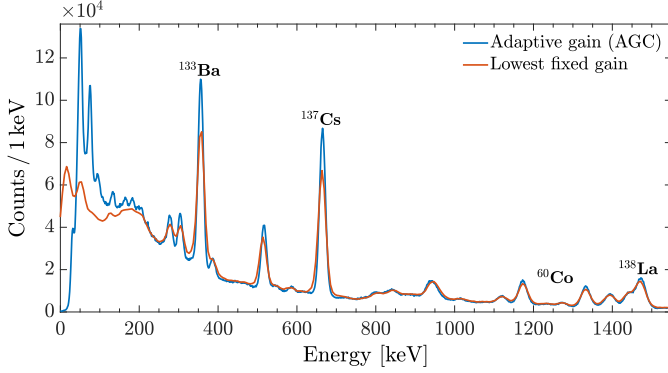
Fig. 4. Comparison between the spectra obtained with AGC and with the lowest fixed gain. The cosmic rays endpoint [full-scale range (FSR)] is around 30 MeV (not visible in the figure). (a) Spectrum obtained with AGC and the one obtained with the lowest fixed gain are superimposed. (b) Below 1 MeV AGC features a clearly better resolution than the lowest fixed gain.
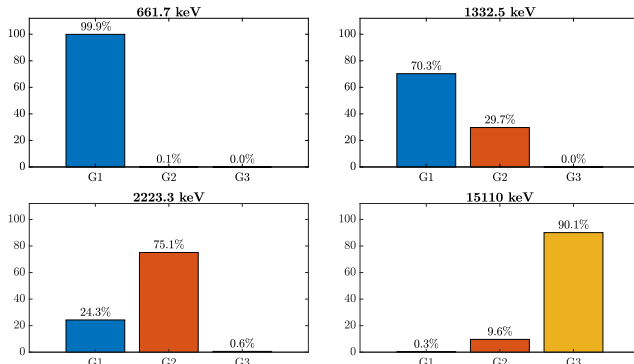

Fig. 5. Histograms show the usage trend of the three gains for four peaks spanning from 661.7 keV to 15.11 MeV.

possible performance under all circumstances removing the trade-off between resolution and energy dynamic range.

B. Spectrum Linearity

The main factor causing non-linearity in the spectrum is the saturation of the SiPMs. An SiPM is indeed constituted by the parallel connection of elementary cells [single photon avalanche diodes (SPADs)], and its output signal depends, in first approximation, on the number of photons impinging on the active area. But, when the number of photons is large and comparable to the total number of cells, the probability that two or more photons hit the same cell rises. An SPAD is not able to detect further photons after the first one if they

TABLE II
SUMMARY OF THE SIMULATED NON-LINEARITY AND THE MEASURED ONE FOR SOME PEAKS OF INTEREST (WITH AGC ON)

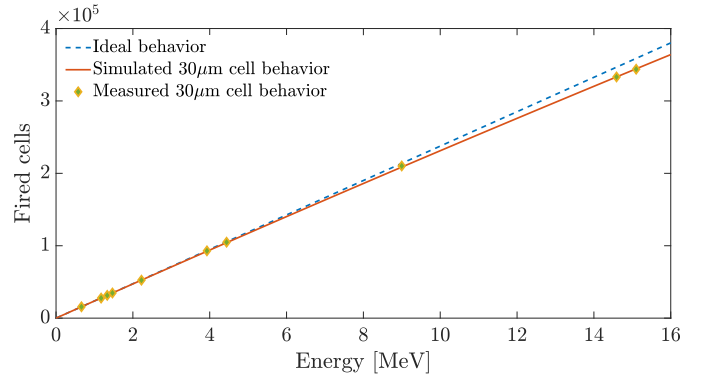| Energy [keV]	Measured non-lin.	Simulated non-lin.	Delta [keV]	Resolution [keV]
662	-0.2%	-0.2%	0.0	17.9
1173	-0.6%	-0.3%	3.5	23.5
1332	-0.6%	-0.4%	2.7	24.0
1468	-0.4%	-0.4%	0.0	n/a
2223	-0.7%	-0.6%	2.2	37.8
3927	-0.4%	-1.1%	27.5	n/a
4438	-0.5%	-1.2%	31.1	108
8998	-1.7%	-2.4%	63.0	86.2
14599	-3.9%	-3.9%	0.0	n/a
15110	-4.2%	-4.0%	30.2	181

Fig. 6. Non-linearity of the SiPMs in terms of fired cells with respect to energy. At high energy, the system starts deviating from the linear behavior due to the microcell saturation effect. AGC and G3 behave similarly.

arrive before the recharge time necessary to rearm the cells has elapsed (~100 ns). With fast light pulses, like those generated by lanthanum bromide scintillators, the situation described above is common, and therefore the photons impinging the same cell after the first one do not contribute to the signal output: they are lost and not counted. The number of fired cells N_{fired}, taking into account the aforementioned phenomenon, can be computed as proposed by [25]

$$N_{\text{fired}} = N_{\text{tot}} \cdot \left(1 - e^{-\frac{\text{PDE} \cdot N_{\text{ph}}}{N_{\text{tot}}}} \right) \quad (1)$$

where the number of impinging photons N_{ph} is determined knowing the yield of the scintillator crystal, the energy of the γ-ray, and the dead area between the SiPMs, while the total number of cells N_{tot} can be computed starting from the area of the scintillator window, the density of the SPADs, and again taking into account the dead space between each SiPM. The last parameter necessary to be able to calculate a priori the non-linearity is the photon detection efficiency (PDE) that, taking into account also the resin used to cover the SiPMs, has been measured, and it is equal to 38% at the wavelength of interest (~385 nm).

Table II lists the simulated and measured non-linearity for different energies, while in Fig. 6, the non-linearity expressed in terms of fired cells is depicted. The simulation has been performed using SiPMs with 30 μm cells coupled with a 3" × 3" LaBr$_3$:Ce:Sr.
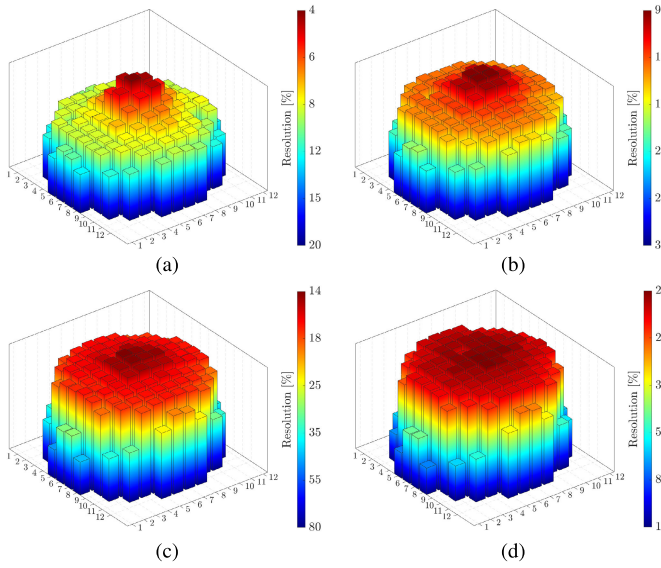
Fig. 7. 3-D bar plots for four different energies, showing per-SiPM resolutions trend at the optimal fixed gain. (a) 15 110 keV peak. (b) 4438 keV peak. (c) 1332 keV peak. (d) 662 keV peak.

From Table II, it can be deduced that (1) does not completely eliminate the non-linearity. This is expected since, in particular at energies where the SiPMs saturation is negligible, other factors contribute more to the non-linearity due to the electronics and to the crystal itself. However, this relation may provide a first-order correction that makes a SiPM-read crystal much more linear than a PMT-read one.

C. Per-SiPM Resolution

Thanks to the 144 independently read SiPMs, it is possible to perform per-SiPM analyses. In particular, the FWHM resolution of a peak of interest can be computed individually for each SiPM. But it must be kept in mind that the peak of interest is not visible in the spectrum of a single SiPM. This is due to the degraded resolution resulting from the limited amount of light of an event received from a single SiPM. Therefore, the peak needs to be gated in the spectrum created from the sum of all the SiPMs and then the corresponding events extracted. From these events, a new per-SiPM spectrum can be generated, and the resolution computed. A 3-D plot is useful to visualize the trend of the resolutions just calculated.

In Fig. 7(a), the selected peak is the full-energy peak (FEP) at 15 110 keV. It is evident how the per-SiPM resolution worsens passing from the central SiPMs of the matrix to the outer ones.

If, instead, we look at Fig. 7(b)–(d), we realize how this trend is less and less perceptible as the energy of the peak under examination decreases.

The origin of this phenomenon is still not completely understood, but it is speculated that it is somehow related to the different interaction positions of the γ-photons inside the crystal, which changes with the energy and, therefore, with the depth of absorption of the γ-rays inside the crystal.

D. Relativistic Doppler Effect Correction

γ-rays at 15.11 MeV energy, produced by a boron-on-deuterium beam, are subject to relativistic Doppler broadening.
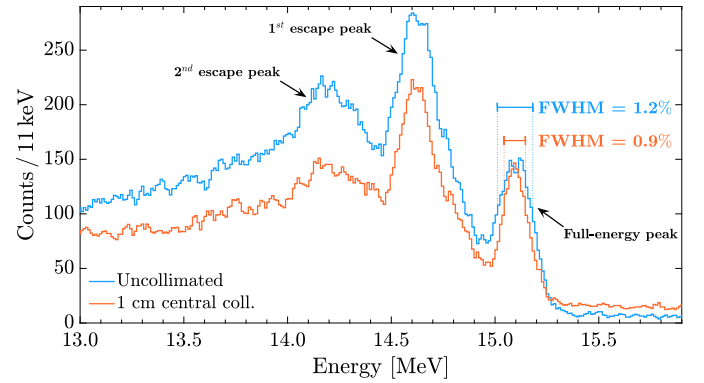

Fig. 8. Direct comparison between the collimated measurement and the uncollimated one. The maximum obtainable improvement by correcting the Doppler broadening is around 25%.

This is due to the high moving velocity of the carbon nucleus that emits the γ-rays. The goal of the measurements was to maximize this phenomenon to investigate the possibility of reducing its magnitude by exploiting the imaging capabilities of the system, made possible by the pixelated nature of the SiPM matrix. The Doppler broadening was maximized by placing the detector at 90° with respect to the direction of the boron beam and 21 cm apart from the deuterium target, as depicted in Fig. 2. Eight collimated measurements have been performed as described in Section III and depicted in Fig. 3. The only unknown information needed to compensate for the Doppler effect in an uncollimated measurement is the angle ϑ of the γ-rays with respect to the beam axis. To compute the aforementioned angle, the first interaction point of the γ-rays inside the crystal needs to be determined. This can be done by exploiting ML algorithms.

Before trying to compensate for the Doppler broadening, an estimate of the possible correction has been done. The maximum obtainable improvement in resolution is around 25%, as shown in Fig. 8 where a 1-cm collimated and the uncollimated measurement have been compared. The two measurements are normalized with respect to the number of events at the maximum of the full-energy peak. The duration of the uncollimated acquisition was 4 h. Instead, it took more than 12 h to reach the same number of peak events for the collimated one. This explains the large amount of high-energy events due to cosmic rays in the collimated acquisition. During measurements lasting several hours and performed in an uncontrolled environment, it is essential to enable the so-called "Auto HV" function of the system [2] that ensures the tracking of temperature changes of the SiPMs and accordingly adjusts their bias voltage. The breakdown voltage of an SiPM is indeed temperature dependent and influences its gain: unwanted gain variations cause shifts in the peaks of the spectrum, severely worsening the energy resolution.

Then, the datasets acquired with the 1 cm collimation have been compared to the uncollimated one calculating the ratio between the average signal of each SiPM channel. In this comparison, only the events of the full-energy peak have been selected. The purpose is to verify if there are different lighting patterns on the SiPMs in the collimated measurements compared to the uncollimated measurement that can be exploited by the ML algorithms to assign the events to
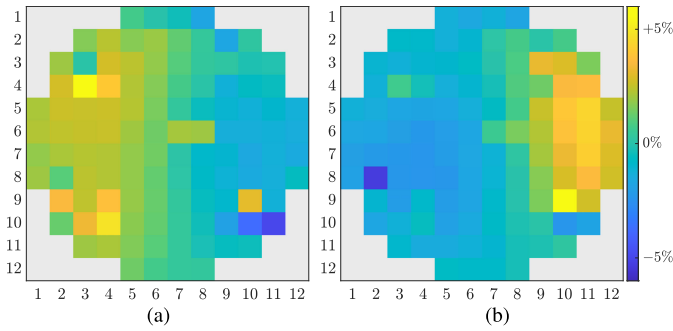
Fig. 9. (a) Left slice (position number 4). (b) Extreme right slice (position number 1). In the 1 cm collimated measurements, the average number of photons is greater in the area not covered by the collimator if compared with the uncollimated measurement.

TABLE III

CORRECTION COEFFICIENTS CALCULATED FROM (2) FOR THE FIVE POSITIONS VISIBLE IN FIG. 3(a). NOTICE THAT ALSO FOR THE CENTRAL POSITION (NUMBER 3), THE COEFFICIENT IS NOT 1: THIS IS EXPECTED SINCE AT AN ANGLE OF 90° THERE IS A SMALL RED-SHIFT OF THE MEASURED ENERGY

	Pos. 1	Pos. 2	Pos. 3	Pos. 4	Pos. 5
Angle	83.2°	86.6°	90.0°	92.3°	95.7°
Correction coefficient	0.9955	0.9983	1.0012	1.0031	1.0059

the correct class out of the five available (one for each of the five 1 cm collimated measurements). The results confirming the presence of an illumination pattern that depends on the irradiation position are visible in Fig. 9 for the positions labeled as numbers 4 and 1 when referring to the ones shown in Fig. 3(a).

The ML algorithm selected to reconstruct the position of the first interaction is the k nearest neighbor (k-NN) pattern recognition algorithm [26], because it demonstrated the most reliable results in this use case. The training datasets for the k-NN were created with the five 1 cm collimated measurements. The trained algorithm was then tested with the three 2 cm collimated measurements. Knowing the exact position of the slices with 1 cm collimation and the distance of the detector from the deuterium target, five possible angles of incidence of the γ-rays with the crystal have been calculated. From these five angles, knowing that $v/c \simeq 0.048$ during the measurements, we can obtain the correction coefficients (E_γ^0/E_γ) to be applied to every single event (shown in Table III), once the interaction position is known, by using the formula

$$E_\gamma = E_\gamma^0 \cdot \frac{\sqrt{1 - \frac{v^2}{c^2}}}{1 - \frac{v}{c}\cos\vartheta} \qquad (2)$$

where E_γ is the measured energy (lab frame), E_γ^0 is the gamma-ray energy in the rest frame, and θ is the incidence angle as defined in Fig. 2.

Lastly, exploiting the k-NN algorithm, the position of interaction of the events generated from the boron on deuterium reaction in the uncollimated measurements has been calculated, and the coefficients for the correction applied. The result, depicted in Fig. 10(a), shows a peak that has slightly moved
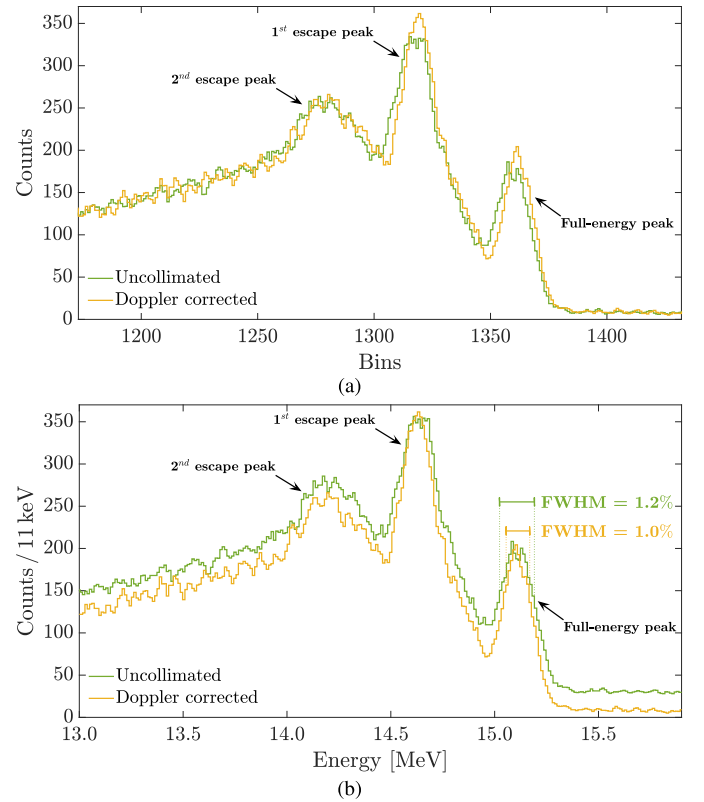

Fig. 10. Doppler corrected spectra with the x-axis in ADC bins (a) and with the x-axis calibrated in energy (b). (a) In this spectrum, the Doppler correction has been applied to the FEP, the 1EP, and the 2EP. (b) Uncollimated measurement has been shifted to the right and moved upward to highlight the differences between the two FEPs. As can be seen, the resolution has improved by about 15% in the Doppler corrected measurement.

to higher energy (about 2 bins, corresponding to 20 keV); this is expected because the GAMMA detector has been placed at 90° with respect to the deuterium target. Indeed, using $\vartheta = 90°$ in (2), we obtain that the centroid of the FEP should be around 15 082 keV before the Doppler correction. Finally, the FWHM resolution of the new peak has been calculated by removing the background, and it is equal to 1.02%. There is, therefore, an improvement of roughly 15% compared to the uncollimated measurement. To better visualize the gain in resolution and allow a direct comparison with Fig. 8, the uncollimated measurement has been shifted upward so that the two FEPs have roughly the same number of events at the maximum point. Furthermore, both peaks have been calibrated with an energy of 15 110 keV in order to have the same centroid. The obtained spectrum is shown in Fig. 10(b).

In Fig. 10(a) and (b), the uncollimated measurement has a duration of 5 h, instead in Fig. 8 its duration has been reduced to 4 h to obtain a comparison with the collimated measurement. For this reason, the two spectra are slightly different.

V. CONCLUSION

With these measurements, the first ever reported at such high energy and wide dynamic range with SiPMs, the GAMMA detector confirms its capabilities in reaching a state-of-the-art resolution with an energy dynamic range from hundreds

of keV to tens of MeV. Also, the predictable non-linearity of SiPMs, due to geometrical reasons, is a great advantage compared to PMTs. Indeed, the latter exhibit non-deterministic linearity, especially for high-energy γ-rays [27]. The pixelated nature of the detection surface allows the reconstruction of the γ-ray interaction point inside the crystal, thus the correction of the relativistic Doppler broadening. Furthermore, it makes possible per-SiPM analyses, which allow studying the interaction of γ-rays at different energies with the scintillator.

REFERENCES

[1] F. Simon, "Silicon photomultipliers in particle and nuclear physics," *Nucl. Instrum. Methods Phys. Res. A, Accel. Spectrom. Detect. Assoc. Equip.*, vol. 926, pp. 85–100, May 2019.

[2] D. Di Vita et al., "A 144-SiPM 3" LaBr$_3$ readout module for PMTs replacement in Gamma spectroscopy," *Nucl. Instrum. Methods Phys. Res. A, Accel. Spectrom. Detect. Assoc. Equip.*, vol. 1040, pp. 1–6, Oct. 2022.

[3] C. Mihai et al., "Development of large area silicon photomultipliers arrays for γ-ray spectroscopy applications," *Nucl. Instrum. Methods Phys. Res. A, Accel. Spectrom. Detect. Assoc. Equip.*, vol. 953, Jan. 2020, Art. no. 163263.

[4] R. Sariyal, I. Mazumdar, and S. M. Patel, "Measurement of absolute light yield and quantum efficiency of LaBr$_3$:Ce scintillator detector using SiPM," *J. Instrum.*, vol. 16, no. 12, Dec. 2021, Art. no. P12024.

[5] G. L. Montagnani et al., "Spectroscopic performance of a Sr co-doped 3" LaBr$_3$ scintillator read by a SiPM array," *Nucl. Instrum. Methods Phys. Res. A, Accel. Spectrom. Detect. Assoc. Equip.*, vol. 931, pp. 158–161, Jan. 2019.

[6] A. Gola et al., "NUV-sensitive silicon photomultiplier technologies developed at fondazione Bruno Kessler," *Sensors*, vol. 19, no. 2, p. 308, Jan. 2019.

[7] O. Poleshchuk et al., "Performance tests of a LaBr$_3$:Ce detector coupled to a SiPM array and the GET electronics for γ-ray spectroscopy in a strong magnetic field," *Nucl. Instrum. Methods Phys. Res. A, Accel. Spectrom. Detect. Assoc. Equip.*, vol. 987, Jan. 2021, Art. no. 164863.

[8] G. Ticchi et al., "Embedded artificial intelligence for position sensitivity in thick scintillators," *Nucl. Instrum. Methods Phys. Res. Sect. A, Accel., Spectrometers, Detectors Associated Equip.*, vol. 1041, pp. 1–5, Oct. 2022.

[9] L. Buonanno et al., "Real-time imaging with thick LaBr$_3$: FPGA-embedded machine and deep learning for nuclear physics," in *Proc. IEEE Nucl. Sci. Symp. Med. Imag. Conf. (NSS/MIC)*, Oct. 2021, pp. 1–3.

[10] A. Razeto et al., "Very large SiPM arrays with aggregated output," *J. Instrum.*, vol. 17, no. 5, May 2022, Art. no. P05038.

[11] C. E. Aalseth et al., "Darkside-20k: A 20 tonne two-phase LAr TPC for direct dark matter detection at LNGS," *Eur. Phys. J. Plus*, vol. 133, no. 3, pp. 1–129, 2018.

[12] P.-A. Söderström et al., "Design and construction of a 9 MeV γ-ray source based on capture of moderated plutonium–beryllium neutrons in nickel," *Appl. Radiat. Isot.*, vol. 191, Jan. 2023, Art. no. 110559.

[13] J. G. Rogers, M. S. Andreaco, C. Moisan, and I. M. Thorson, "A 7–9 MeV isotopic gamma-ray source for detector testing," *Nucl. Instrum. Methods Phys. Res. A, Accel. Spectrom. Detect. Assoc. Equip.*, vol. 413, nos. 2–3, pp. 249–254, Aug. 1998.

[14] L. Buonanno, D. D. Vita, M. Carminati, and C. Fiorini, "GAMMA: A 16-channel spectroscopic ASIC for SiPMs readout with 84-dB dynamic range," *IEEE Trans. Nucl. Sci.*, vol. 68, no. 10, pp. 2559–2572, Oct. 2021.

[15] H. J. Wollersheim et al., "Rare isotopes investigation at GSI (RISING) using gamma-ray spectroscopy at relativistic energies," *Nucl. Instrum. Methods Phys. Res. A*, vol. 537, no. 3, pp. 637–657, 2005.

[16] N. Blasi et al., "Position sensitivity in large spectroscopic LaBr$_3$:Ce crystals for Doppler broadening correction," *Nucl. Instrum. Methods Phys. Res. A, Accel. Spectrom. Detect. Assoc. Equip.*, vol. 839, pp. 23–28, Dec. 2016.

[17] I. Burducea, D. G. Ghiţă, T. B. Sava, and M. Straticiuc, "Tandem accelerators in Romania: Multi-tools for science, education and technology," in *Proc. AIP Conf.*, 2017, Art. no. 060001.

[18] C. R. Nita et al., "The energy calibration of the bucharest Fn tandem accelerator," *Univ. Politehnica Bucharest Sci. Bull., A-Appl. Math. Phys.*, vol. 74, no. 4, pp. 141–152, 2012.

[19] D. G. Ghiţă et al., "New developments at the Tandem accelerators laboratory at IFIN-HH," in *Proc. HIAT*, 2012, pp. 1–6.

[20] D. Alburger and D. Wilkinson, "γ-ray decay of the 15.11-MeV T = 1 state of ^{12}C," *Phys. Rev. C*, vol. 5, no. 2, p. 384, 1972.

[21] D. P. Balamuth, R. W. Zurmühle, and S. L. Tabor, "Isospin-forbidden alpha decay of the 15.11-MeV state in ^{12}C," *Phys. Rev. C*, vol. 10, no. 3, pp. 975–986, Sep. 1974.

[22] J. Kelley, J. Purcell, and C. Sheu, "Energy levels of light nuclei A=12," *Nucl. Phys. A*, vol. 968, pp. 71–253, Jan. 2017.

[23] O. B. Tarasov and D. Bazin, "LISE++: Radioactive beam production with in-flight separators," *Nucl. Instrum. Methods Phys. Res. Sect. B, Beam Interact. Mater. At.*, vol. 266, nos. 19–20, pp. 4657–4664, Oct. 2008.

[24] A. Gavron, "Statistical model calculations in heavy ion reactions," *Phys. Rev. C*, vol. 21, no. 1, pp. 230–236, Jan. 1980. [Online]. Available: https://lise.nscl.msu.edu/pace4.html

[25] D. Renker and E. Lorenz, "Advances in solid state photon detectors," *J. Instrum.*, vol. 4, no. 4, pp. 1–54, 2009.

[26] T. Cover and P. Hart, "Nearest neighbor pattern classification," *IEEE Trans. Inf. Theory*, vol. IT-13, no. 1, pp. 21–27, Jan. 1967.

[27] G. Gosta et al., "Response function and linearity for high energy γ-rays in large volume LaBr$_3$:Ce detectors," *Nucl. Instrum. Methods Phys. Res. A, Accel. Spectrom. Detect. Assoc. Equip.*, vol. 879, pp. 92–100, Jan. 2018.